An Improved TES Method to Retrieve Urban Surface Temperature

Zhu, Lili; Yang, Jinxin; Ouyang, Xiaoying; Shi, Qian; Xu, Yong; Wong, Man Sing; Menenti, Massimo

DOI
10.1109/TGRS.2025.3642812

Publication date
2025

Document Version
Final published version

Published in
IEEE Transactions on Geoscience and Remote Sensing

Citation (APA)
Zhu, L., Yang, J., Ouyang, X., Shi, Q., Xu, Y., Wong, M. S., & Menenti, M. (2025). An Improved TES Method to Retrieve Urban Surface Temperature. *IEEE Transactions on Geoscience and Remote Sensing*, *63*, Article 5010813. https://doi.org/10.1109/TGRS.2025.3642812

An Improved TES Method to Retrieve Urban Surface Temperature

Lili Zhu, Jinxin Yang, Xiaoying Ouyang, Qian Shi, *Senior Member, IEEE*, Yong Xu, Man Sing Wong, and Massimo Menenti

***Abstract*—The urban complex material and geometry characteristics result in a 3-D thermal heterogeneity and that limits the urban surface temperature (UST) retrieval. In this study, we improved the temperature and emissivity separation (TES) algorithm by incorporating thermal heterogeneity within mixed pixel (MP). The improvement was based on the discrete anisotropic radiative transfer (DART) model and applied to retrieve land surface temperature (LST) from Sustainable Development Goals Science Satellite 1 (SDGSAT-1). The TES algorithm retrieval approach for MP (TES-MP) algorithm was validated with ECOsystem Spaceborne Thermal Radiometer Experiment on Space Station (ECOSTRESS) and the data simulated by the DART model, and the results show that it can reach good accuracy under complex urban conditions. Based on the simulated scenes from the Sheung Wan building in Hong Kong, the root mean squared error (RMSE) of the TES-MP algorithm is 0.85 K under thermal homogeneous conditions and 1.13 K under thermal heterogeneous conditions. Additionally, new high-reflectivity construction materials are common in urban areas, i.e., metal materials. It shows that the relationship between maximum-minimum difference (MMD) and minimum emissivity ($\varepsilon_{\min}$) is not applicable to these materials. Thus, the impacts of such materials on the UST retrieval were evaluated. The results show that the higher the reflectivity and the fractional abundance of such materials, the larger the LST underestimation. Under nadir observation conditions, the proportion of high-reflectivity walls does not cause significant LST retrieval errors. The geometry and adjacency effects on retrieved LST were evaluated, and the results show that the TES-MP algorithm has some resistance to geometry and adjacency effects, thereby reducing errors in LST retrieval. This study provides a new view on retrieving LST of urban MPs and also suggests that three or more bands should be considered when setting up thermal infrared (TIR) sensors.**

***Index Terms*—Discrete anisotropic radiative transfer (DART), mixed pixel (MP), Sustainable Development Goals Science Satellite 1 (SDGSAT-1), temperature and emissivity separation (TES) algorithm, urban geometry, urban surface temperature (UST).**

I. Introduction

URBAN surface temperature (UST) is a key variable determining urban energy balance and urban microclimate [1], [2], [3]. With the growth of urbanization, urban land surface materials and geometries significantly influence urban energy balance [4]. Monitoring UST is important to understand urban climate and environment [5], [6].

Satellite-based thermal infrared (TIR) data are the only way to capture regional patterns in UST and thus has been widely used for studying UST across temporal and spatial scales [7], [8], [9], [10]. Numerous studies have been dedicated to develop algorithms to retrieve land surface temperature (LST) from thermal remote sensing (RS) [11]. For flat and homogeneous natural surface, current algorithms of LST retrieval can reach ideal accuracy, and root mean squared error (RMSE) is lower than 2 K [12], [13]. Urbanization development makes urban geometry and material heterogeneity more complex. Particularly, this implies that multiple scattering and adjacency effects cannot be neglected [14]. A widely used approach to retrieve UST involves considering the impact of geometry, utilizing the sky view factor (SVF) to account for multiple scattering and adjacency effects. Yang et al. [15] developed an urban emissivity, single-channel (SC) model based on the SVF (IUEM-SVF), which also accounted for adjacency effects. Chen et al. [16] developed an urban split-window (USW) algorithm to retrieve UST with high spatial resolution TIR data from the visible and infrared multispectral sensor (VIMS) onboard Chinese GaoFen-5 (GF-5) satellite, by removing the geometry, adjacency, and atmospheric effects based on SVF. Chen et al. [4] developed a similar urban temperature and emissivity separation (TES) algorithm, and results showed that the magnitude of the geometry effects on UST were approximately 3.2, 4.2, 4.0, and 3.9 K for the four GF-5 TIR bands. These studies are based on algorithms developed on pure pixels (PPs), despite considering the influence of urban geometry.

Received 16 July 2025; revised 11 November 2025; accepted 4 December 2025. Date of publication 11 December 2025; date of current version 22 December 2025. This work was supported in part by the National Natural Science Foundation of China under Grant 42222106, Grant 42271345, Grant 42171370, and Grant 42271477; in part by the Otto Poon Research Institute for Climate-Resilient Infrastructure, Research Institute for Sustainable Urban Development, Research Institute of Land and Space, The Hong Kong Polytechnic University, Hong Kong, China, under Grant N-ZH8S, Grant BBG2, and Grant 1-CDL5; in part by the General Research Fund under Grant 15603923 and Grant 15609421; in part by the Collaborative Research Fund under Grant C5062–21GF; and in part by the Young Collaborative Research Fund from the Research Grants Council, Hong Kong, China, under Grant C6003–22Y. *(Corresponding authors: Jinxin Yang; Xiaoying Ouyang.)*

Lili Zhu, Jinxin Yang, and Yong Xu are with the School of Geography and Remote Sensing, Guangzhou University, Guangzhou 510006, China, and also with the School of Huangpu Research, Guangzhou University, Guangzhou 510700, China (e-mail: zhull@e.gzhu.edu.cn; yangjx11@gzhu.edu.cn; xu1129@gzhu.edu.cn).

Xiaoying Ouyang is with the International Research Center of Big Data for Sustainable Development Goals, Beijing 100094, China, and also with the Aerospace Information Research Institute, Chinese Academy of Sciences, Beijing 100094, China (e-mail: ouyxy@aircas.ac.cn).

Qian Shi is with the School of Geography and Planning, Sun Yat-sen University, Guangzhou 510006, China, and also with Guangdong Provincial Key Laboratory for Urbanization and Geo-simulation, Guangzhou 510275, China (e-mail: shixi5@mail.sysu.edu.cn).

Man Sing Wong is with the Department of Land Surveying and Geo-Informatics, The Hong Kong Polytechnic University, Hong Kong, China (e-mail: ls.charles@polyu.edu.hk).

Massimo Menenti is with the Institute for Tibetan Plateau Research, Chinese Academy of Sciences, Beijing 100094, China, and also with the Faculty of Civil Engineering and Earth Sciences, Delft University of Technology, 2600 GA Delft, The Netherlands (e-mail: m.menenti@tudelft.nl).

Digital Object Identifier 10.1109/TGRS.2025.3642812

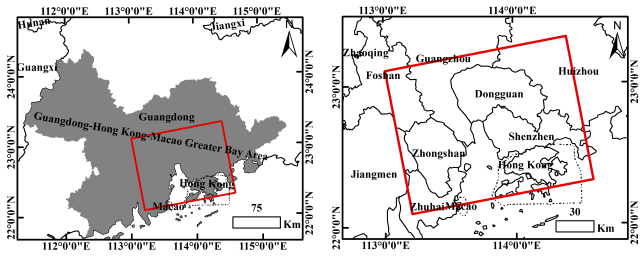

Fig. 1. Study area (red line zone).

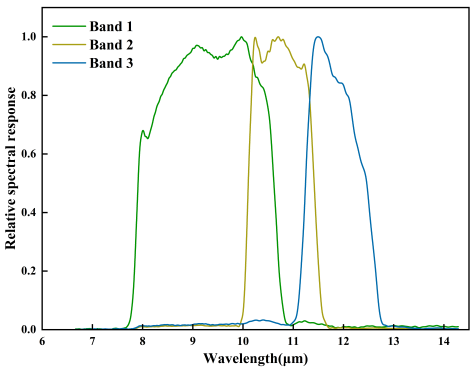

Fig. 2. Spectral response function of SDGSAT-1 TIR.

TABLE I
ACQUISITION TIME OF SDGSAT-1 TIR SCENES

Count	Time	Location
1	2024-2-10 21:42	Lower Pearl River Delta
2	2024-5-16 21:38	Lower Pearl River Delta
3	2024-12-31 9:56	Lower Pearl River Delta
4	2025- 5-27 21:13	Central Shijiazhuang

Additionally, urban materials exhibit high heterogeneity, making it challenging to estimate emissivity. Compared with other UST retrieval methods, the temperature emissivity separation algorithm can deal with the uncertainty of emissivity. In [4], an empirical relationship between the minimum emissivity ($\varepsilon_{\min}$) and maximum–minimum difference (MMD) for urban areas was developed by considering multiple scattering under the assumption of homogeneous material emissivity. This relationship achieves high accuracy when applied to high spatial resolution data. When using intermediate spatial resolution data, it is hard to find any PP in urban areas. Due to lower spatial resolution of TIR satellite data, mixed pixels (MPs) always exist and emissivity within a pixel is variable [17]. For MPs in urban areas, the interaction among heterogeneous components within each pixel and with the surrounding pixels cannot be neglected [15]. Therefore, a specific empirical relationship between $\varepsilon_{\min}$ and MMD should be developed by considering these interactions when applying TES algorithm to retrieve UST using intermediate and low spatial resolution data.

In this study, we proposed a TES algorithm retrieval approach for MP (TES-MP). Traditional models are difficult to simulate the interaction of the mixed elements, so the discrete anisotropic radiative transfer (DART) model was employed in this study. DART can simulate the interactions between complex surfaces and subsequently generate the resulting outputs. To develop the relationship between $\varepsilon_{\min}$ and MMD for urban MPs, DART was employed to simulate TIR under heterogeneous thermal and emissivity conditions, with building density (BD) and height (BH) held constant within each scene. TES-MP algorithm was validated in a portion of the Mong Kok (Hong Kong) and evaluated in a portion of the Sheung Wan (Hong Kong) using the DART, accounting for the effects of high reflectivity, geometry, and adjacency. In this study, the Sustainable Development Science Satellite 1 was used to retrieve UST. Sustainable Development Goals Science Satellite 1 (SDGSAT-1) has three TIR bands (8–10.5, 10.3–11.3, and 11.5–12.5 μm) with a spatial resolution of 30 m [18], making it suitable for UST retrieval using the TES-MP algorithm. Subsequently, the results were validated against LST data from ECOsystem Spaceborne Thermal Radiometer Experiment on Space Station (ECOSTRESS) in the central Shijiazhuang.

II. Study Area and Data

A. Study Area

The study area is located in the Pearl River Delta Plain (Fig. 1), covering the southern region of Guangzhou, the southeastern region of Foshan, the entirety of Zhongshan and Dongguan, parts of Zhuhai and Macao, most of Shenzhen and Hong Kong, as well as small portions of Huizhou and Jiangmen. This area encompasses the majority of Guangdong–Hong Kong–Macao Greater Bay Area and serves as the core region for economic development [19].

B. TIR Data

1) SDGSAT-1 TIR: SDGSAT-1 is dedicated to serving the 2030 Agenda for SDGs [20], and it was launched on November 5, 2021. It can collect TIR data day and night with a 30-m spatial resolution, covering the globe in 11 days [2]. It has three TIR bands (8–10.5, 10.3–11.3, and 11.5–12.5 μm), and the spectral response functions of these bands are shown in Fig. 2. In this study, the three TIR scenes (Table I) were applied in the lower Pearl River Delta.

2) ECOSTRESS TIR: The ECOSTRESS was launched to the International Space Station (ISS) on June 29, 2018. It has a viewing swath width of approximately 384 km and observes the surface of the Earth from 53.6°N to 53.6°S, with revisit times that vary depending on the ISS orbit [21]. Thus, it may repeatedly observe per day in some areas and it has five TIR bands and one shortwave infrared band with 70-m spatial resolution. Due to the lack of on-site measurements, this study used the ECOSTRESS L2 LST product [22] to validate the SDGSAT-1 retrievals, which is a reliable procedure [23].

Cloud cover in the Pearl River Delta Plain is generally large and frequent, leading to limited availability of TIR images. To validate our approach, we selected central Shijiazhuang on May 27, 2025. The LST of SDGSAT-1 was resampled

to 70-m resolution using the average resampling method to align with the spatial resolution of ECOSTRESS. On that day, ECOSTRESS data over Shijiazhuang was acquired at 8:37 P.M., and SDGSAT-1 data at 9:13 P.M. Despite the half-hour gap between data collections, nighttime surface temperature variations are relatively small [24], enabling a valid comparison.

C. Spectral Library

The ECOSTRESS spectral library is a compilation of over 3400 spectra of natural and man-made materials. It includes data from three other spectral libraries (e.g., JHU, JPL, and USGS-Reston), and it is an extension and update of the ASTER spectral library [25].

Spectral databases were essential for this study, and we selected 77 materials from the ECOSTRESS spectral library, comprising man-made materials, rocks, and trees.

Since there are few man-made samples in the ECOSTRESS database, we conducted sensitivity tests by incorporating the Spectral Library of Impervious Urban Materials (SLUM) [26], which is based on emissivity measurements taken at the surface in London.

D. Atmospheric Data

ERA5 (https://cds.climate.copernicus.eu/) is the fifth-generation European Centre for Medium-Range Weather Forecasts (ECMWF) reanalysis dataset on global climate and weather for the past eight decades. The ERA5 hourly data provide 37 pressure levels, geopotential, relative humidity, and air temperature with a resolution of 0.25°, and it can be freely downloaded [27]. Moderate resolution atmospheric transmission (MODTRAN 5.2) was combined to estimate atmospheric variables, including upward atmospheric radiance, downward atmospheric radiance, and atmospheric transmittance. Additionally, it was used to correct the TIR data for atmospheric effects.

The resolution of ERA5 is 0.25°, while SDGSAT-1 has a resolution of 30 m. Consequently, bilinear interpolation was applied to resample the atmospheric data to 30-m resolution [28].

The thermodynamic initial guess retrieval (TIGR) dataset is a climatological library of 2311 atmospheric situations representative of the Earth's atmosphere [29]. Any layer in the TIGR dataset with relative humidity exceeding 90%, or two consecutive layers with relative humidity exceeding 85%, or relative humidity exceeding 80% within 2 km of the surface is excluded [30]. The remaining 946 profiles were designated as clear-sky profiles. Water vapor content (WVC) ranged from 0.05 to 8 g/cm^2 and the lower boundary temperature was between 231.25 and 314.16 K.

E. Building Data

This study utilized building data to present real scenes, and we selected a portion of Hong Kong as the study area due to the highly accurate digital surface model (DSM) and building data provided by Hong Kong Lands and Planning Departments. Furthermore, Hong Kong's extremely high BD and complex 3-D urban geometry render it highly suitable as a case study.

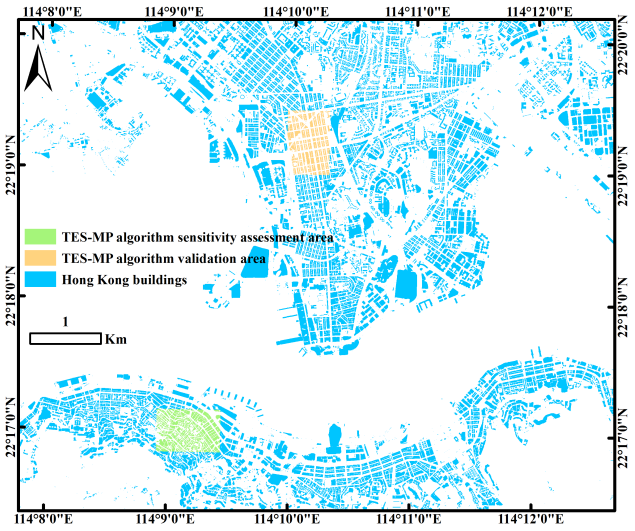

Fig. 3. Shapefile of Hong Kong buildings: the green region represents a portion of Sheung Wan, and the orange region represents a portion of Mong Kok.

The original building data did not include height information of most buildings; DSM data for building locations were used to extract height information. Fig. 3 shows that the Mong Kok (600 × 900 m) and Sheung Wan (900 × 600 m) portions of Hong Kong were used as DART simulation areas. The Mong Kok portion was used as a validation area for the TES-MP algorithm, while the Sheung Wan portion was selected as the sensitivity test area for the TES-MP algorithm. This selection was based on the SVF in the Sheung Wan portion, ranging from 0 to 1 when searched within a radius of 100 m.

III. Methods

The thermal heterogeneity within MPs significantly impacts the UST retrieval. Therefore, this study improved the application of TES in UST retrieval by considering the impacts of the geometry and thermal heterogeneity within pixels and in surrounding pixels. The technical flowchart of the methodology is shown in Fig. 4, including four steps.

Step 1: DART model was applied to simulate the radiance of urban MPs in the three SDGSAT-1 TIR bands.

Step 2: An MMD module for MPs with thermal heterogeneity and different geometries was developed and applied to SDGSAT-1 TIR in the Pearl River Delta.

Step 3: The accuracy of LST and land surface emissivity (LSE) was validated by DART. The LST product from ECOSTRESS was used to validate the LST retrieved by the TES-MP algorithm in the central Shijiazhuang.

Step 4: The impacts of materials, geometries, vegetation, and atmospheric uncertainty on the TES-MP algorithm were analyzed. The building shapefile of Hong Kong was applied to simulate the scenes with thermal heterogeneity and geometry characteristics.

A. TES-MP Algorithm

The infrared radiance received by the sensors at the top of atmosphere (TOA) can be simply written as

$$L_{\text{toa}}(i) = L_{\text{canopy}}(i)\,\tau + R^{\uparrow}_{\text{atm}} \tag{1}$$

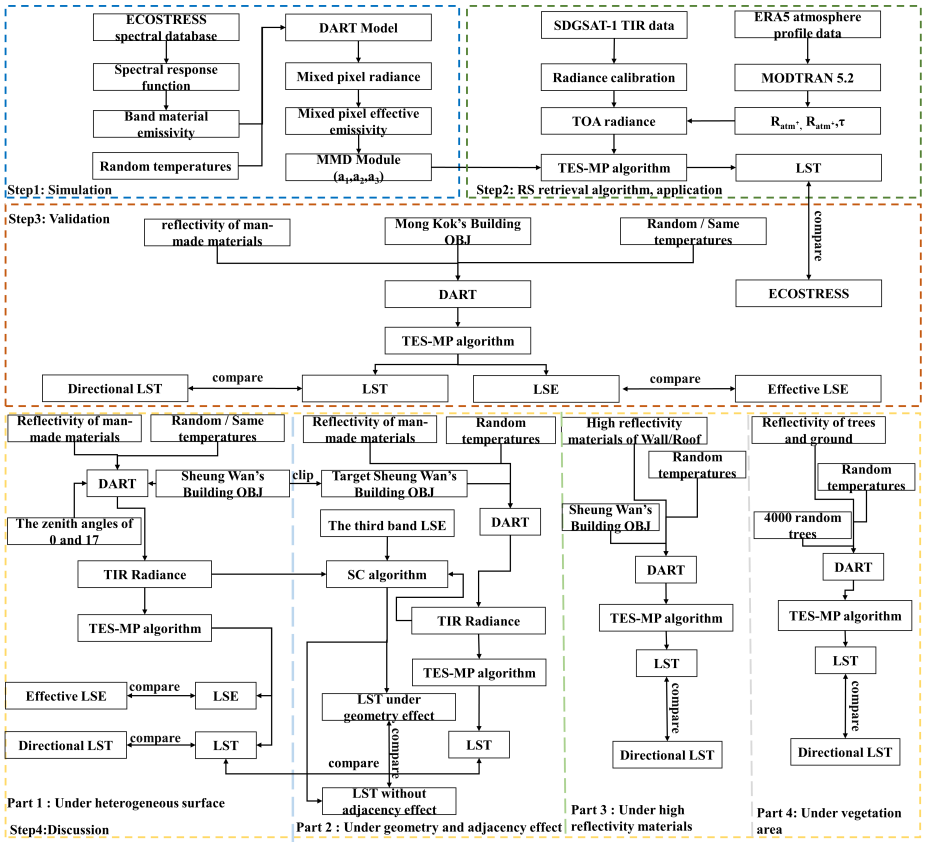

Fig. 4. Flowchart illustrating the processes of MP modeling, surface temperature retrieval, validation, and sensitivity analysis using DART.

where $L_{\text{canopy}}(i)$ is the channel radiance observed for pixel i at ground level, τ is the effective transmittance of the atmosphere, and $R^{\uparrow}_{\text{atm}}$ is the upward atmospheric thermal radiance [31].

The TIR exitance can be written as

$$L_{\text{canopy}}(i) = \varepsilon_i B_i(T_s) + (1-\varepsilon_i) R^{\downarrow}_{\text{atm}} \tag{2}$$

where ε_i is the effective emissivity of the pixel i with geometry and material information, $R^{\downarrow}_{\text{atm}}$ is the atmospheric downward radiance, T_s is the surface temperature of pixel i, and $B_i(T_s)$ is the blackbody radiance at the temperature T_s given by the Planck function [13].

The TES algorithm consists of three primary modules: the normalized emissivity method (NEM), the ratio module (RAT), and the MMD [32]. The MMD module is the most significant part in the TES algorithm. The core of the MMD module is the relationship between MMD and $\varepsilon_{\min}$

$$\varepsilon_{\min} = a_1 - a_2 \text{MMD}^{a_3} \tag{3}$$

where the MMD value is calculated by normalized emissivity in the RAT module

$$\text{MMD} = \max(\beta_i) - \min(\beta_i) \tag{4}$$

$$\beta_i = \varepsilon_i / \bar{\varepsilon} \tag{5}$$

where ε_i is the initial emissivity estimated by the NEM based on the calculated surface-emitting radiation. $\bar{\varepsilon}$ is the average emissivity of all channels. The emissivity of the other channels is calculated as

$$\varepsilon_i = \varepsilon_{\min} \beta_i / \min(\beta_i). \tag{6}$$

RS provides the average surface temperature of components in the observation direction, referred to as the directional temperature [33]. We set the emissivity of the scene to 1 in order to obtain the pixel blackbody radiance in the observation direction using DART, and subsequently applied (9) to calculate the true surface temperature in that direction. In this study, all true surface temperatures were calculated by this method.

We used Planck's law to determine the emittance of a blackbody [4]

$$B_\lambda(T_B) = \frac{C_1}{\lambda^5 \left(e^{\frac{C_2}{\lambda T}} - 1 \right)} \tag{7}$$

where T is the temperature of an MP, $C_1 = 1.191 \times 10^8$ W $\cdot$ μm$^4 \cdot$ sr$^{-1} \cdot$ m^{-2} and $C_2 = 1.439 \times 10^4$ μm $\cdot$ K [1]

To calculate the emissivity of the MP, the scene-averaged $B_\lambda(T_S)$ and the blackbody radiance $B_\lambda(T_B)$ from DART, which were calculated as follows, were used:

$$\varepsilon_\lambda = \frac{B_\lambda(T_S)}{B_\lambda(T_B)} \tag{8}$$

where ε_λ was input into the MMD module to fit a new relationship between MMD and $\varepsilon_{\min}$.

The geometry changes the effective emissivity [14], so it is the effective emissivity that needs to be considered for the retrieval of LSE rather than the material's own emissivity. Since both Mong Kok and Sheung Wan areas have complex geometry, it is necessary to obtain their effective LSE. The pixel blackbody radiance was measured by DART under directional observation conditions (with emissivity set to 1)

and the pixel surface radiance, which were substituted into (8) to obtain the effective LSE values for each band.

The temperature was calculated by the following equation. Here, ε represents either the maximum emissivity obtained after TES iterations or the emissivity derived from a single thermal band. This depends on whether the TES algorithm or an SC algorithm retrieval method is employed [4]

$$T_S = \frac{C_2}{\lambda \ln\left(\frac{C_1 \varepsilon}{\lambda^5 B_\lambda(T_S)} + 1\right)}. \tag{9}$$

B. DART Model

The DART model was developed in 1992; it describes radiative transfer from the ultraviolet to the TIR and models passive and active RS signals of urban and natural landscapes [34]. The model has been applied to simulate the radiation budget (RB) for a broad spectrum of applications, including sun-induced chlorophyll fluorescence (SIF), and diverse RS signals (Lidar, spectroradiometer images) [35]. The DART model uses the temperature and optical properties of each element in the scene as input parameters to simulate the interactions among these elements, thereby generating modeled images.

There are two light modes. The forward light mode (e.g., DART-FT and DART-RC) voxelizes landscapes and traces light with the discrete ordinate method (DOM) or Monte Carlo (MC) methods. The bidirectional light mode (DART-Lux) does not voxelize landscapes (a volume has any shape) and traces light with bidirectional MC methods, which is the most accurate and efficient DART mode [35]. Currently, the DART model has been widely used in many studies [36], [37]. The DART model was used to simulate the TIR images of the MPs, enabling the estimation of the relationship between MMD and $\varepsilon_{\min}$, and validating the TES-MP algorithm in this study.

C. Scene Setting and Simulation

1) MP Scene Setting: In this study, DART 10.2 was employed, and DART-Lux was utilized to simulate the TIR of MPs. To simulate TIRs similar to those of SDGSAT-1, the equivalent central wavelengths (9.35, 10.73, and 11.72 μm) were selected to define spectral bands. The band emissivity of each surface was estimated by convolution of the ECOSTRESS spectral library with the SDGSAT-1 spectral response functions.

In each scene, there were four buildings and the ground, and trees appearing in some scenes. The regular arrangement of buildings and trees is depicted in Fig. 5. The building geometry parameters were set to different BDs and BHs, including five BDs (0.05, 0.25, 0.45, 0.65, and 0.85) and BHs (10, 20, 30, 40, and 50 m) in the simulation scenes (Fig. 5). For each scene, four uniform buildings of the same height were placed. The height of the trees was set to 8 m and the crown diameter to 4.8 m, according to [38]. Trees were added to three BD scenarios: 0.05, 0.25, and 0.45. The number of trees was determined by their structural parameters and the scene dimensions. For the lowest BD scene (0.05), 32 trees were placed; for the other two scenes (0.25 and 0.45), 20 trees were placed. As shown in Fig. 5, there are a total of eight scenes: five tree-free scenes and three tree-added scenes. Different group parameters, such as temperature and emissivity, were assigned in a randomized method, so 5000 groups were simulated.

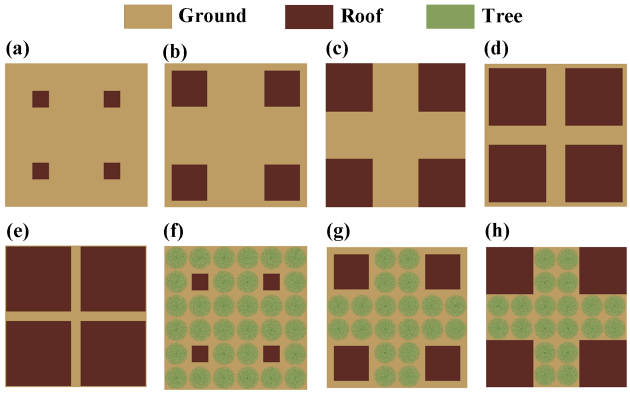

Fig. 5. Top view of the DART-based scene: each scene contains four buildings and a ground surface, with trees present in three of the BD scenes. (a) BD: 0.05, (b) BD: 0.25, (c) BD: 0.45, (d) BD: 0.65, (e) BD: 0.85, (f) BD: 0.05 (trees), (g) BD: 0.25 (trees), and (h) BD: 0.45 (trees).

TABLE II
DART SIMULATION PARAMETERS

Parameters	Parameters
Passive RS &RB	Light propagation mode: Bi-directional
Spectral band	Atmosphere Radiative Transfer (RT): No atmospheric RT (BOA = TOA) Mode: Mode T Central wavelength(μm): 9.35, 10.73, 11.72 Spectral bandwidth(μm): 0 Thermal emission law: Planck
Bi-directional	Maximal scattering order: 200 Target pixel size(m): 1 Number of repetitions of the user-defined scene: 1
Temperature	221K-335K
Products	BRF/BTF
Earth Scene	Earth scene dimensions(m): 30

We referenced the lowest temperature from the filtered clear-sky profiles, with temperature differences ranging from −10 to 20 K, yielding a final temperature range of 221–335 K. Temperature variations for walls, roofs, grounds, and trees within each scene were constrained within ±20 K, with temperatures randomly assigned to each scene. Each scene incorporated up to four different temperatures. Additionally, within each scene, there were four different wall emissivities, four different roof emissivities, one ground emissivity, and a tree emissivity for scenes containing trees. The DART simulation parameters are shown in Table II.

2) TES-MP Algorithm Accuracy Evaluation and Application in DART: To input buildings into the DART model, the buildings' shapefile was converted to OBJ (Fig. 6). To configure MPs in DART, the temperature and emissivity of buildings should be as inconsistent as possible within a pixel.

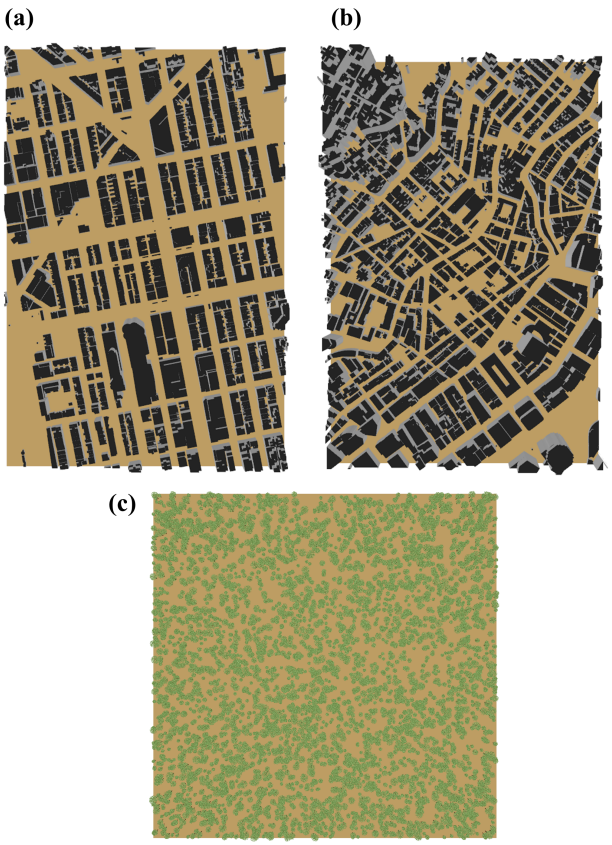

Fig. 6. Top view of the OBJ scene: buildings (roof: black, wall: gray, and ground: yellow). (a) Part of Mong Kok. (b) Part of Sheung Wan. (c) Tree scene (tree: green).

Each building was assigned a unique FID, and most buildings with adjacency FIDs did not occupy the same pixel. Due to limited temperature and emissivity data, we grouped buildings by their FIDs to ensure variability within MPs. We utilized Python to categorize OBJs based on building FIDs into groups, each containing 30 buildings. Within each group, all roofs were assigned one shared ID, and all walls were assigned another shared ID. Finally, the validation area (Mong Kok) and the sensitivity testing area (Sheung Wan) within the DART scene were, respectively, partitioned into 48 and 50 groups.

Given the absence of 3-D surface data and the limitations of DART, we decoupled temperature and reflectance settings from the intrinsic properties of buildings and external environmental factors. This allowed us to independently define the temperature and reflectance for each group. To minimize human subjectivity, temperature and emissivity were assigned through a randomized approach using Python [Fig. 6(a)]. Specifically, the roof temperature ranged from 307 to 335 K, the wall temperature ranged from 305 to 329 K, and the ground temperature was set at 318 K in the validation area. These temperatures were referenced to Hong Kong's high-resolution datetime TIR data in October 2017 and assigned in 1-K increments to avoid minor temperature fluctuations. Given the limited temperature range available for assignment, there may be some overlap of temperatures among different groups. Additionally, a uniform surface temperature scene

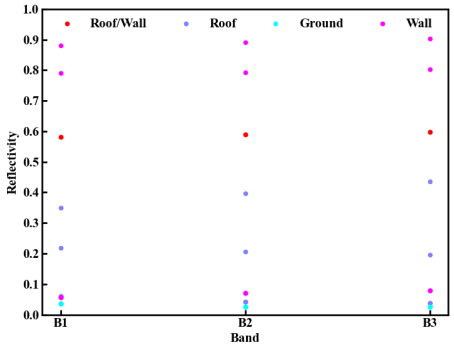

Fig. 7. Reflectivity of walls, grounds, and roofs in three TIR bands.

was considered, with all surfaces set at 300 K. In terms of emissivity, different values were assigned to each group due to the availability of sufficient samples. Notably, one group incorporated high-reflectivity material on the roof, and 20 groups incorporated high-reflectivity materials on the walls.

In the sensitivity test area, the temperature settings were slightly different. We referenced high-resolution datetime TIR data from Hong Kong in October 2017. To create temperature heterogeneity, we assigned different temperatures to the same surface across various groups. The roof temperature ranged from 299 to 350 K at a step of 1 K, the wall temperature ranged from 290 to 341 K at a step of 1 K, and the ground temperature was set at 310 K [Fig. 6(b)]. Additionally, an isothermal scene was simulated, where the same temperature (300 K) was applied to every component shown in Fig. 6(b). This isothermal scene was employed for comparison with the heterogeneous temperature distribution.

To evaluate adjacency effects, all surrounding pixels must be removed from the target pixel. This required subdividing the shapefile into smaller sections. The Sheung Wan area (900 $\times$ 600 m) was subdivided into 600 shapefiles, each measuring 30 $\times$ 30 m. Each building was processed using the method described above: grouped by FIDs and exported as 600 individual OBJ files. By placing the OBJ separately in DART and setting it as a nonrepeating scene for simulation, we ensured that the radiance from each pixel originated exclusively from interactions within that pixel, thereby eliminating adjacency effects.

To analyze the sensitivity of LST retrieved by the TES-MP algorithm in materials with high reflectivity (e.g., metals), three groups of such materials were established. When the roof was designated as high-reflectivity materials, the wall and ground were considered normal materials. Conversely, when the wall was designated as high-reflectivity materials, the roof and ground remained as normal materials (Fig. 7). In the simulation, all outputs were set to 30-m resolution to match the resolution of SDGSAT-1 TIR. Other parameters were the same as Table II. Finally, TES-MP was applied to all simulated TIR images to retrieve LSE and LST.

One important clarification is that the emissivities were randomly assigned and maintained constant, except in the study of the high reflectivity section, where the emissivities of each component were adjusted. This means that, in the experiments at different temperatures and isothermal scenes,

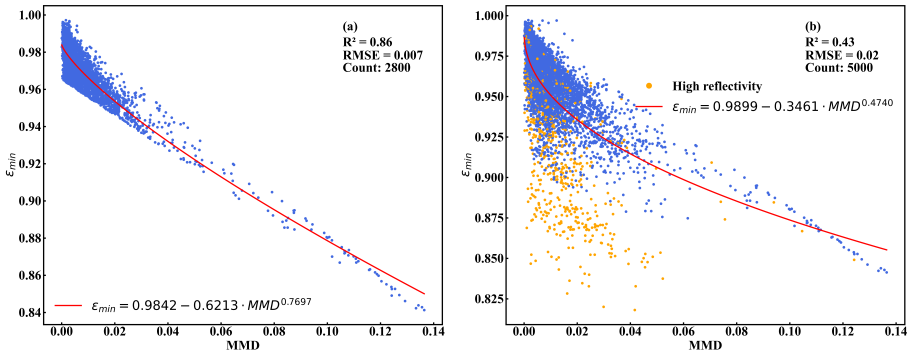

Fig. 8. Relationship between MMD and $\varepsilon_{\min}$: (a) final data and (b) original data.

only the temperatures were varied, while the emissivities remained unchanged.

IV. Results

A. New Relationship Between MMD and $\varepsilon_{\min}$

Fig. 8(a) shows the final relationship between MMD and $\varepsilon_{\min}$, excluding the large percentage of metal materials and the outliers (R^2 = 0.86 and RMSE = 0.007). When including a large percentage of metals and the outliers, the relationship deteriorates significantly.

Fig. 8(b) shows the results for all the simulated data (R^2 = 0.43 and RMSE = 0.02), demonstrating a weak correlation between MMD and $\varepsilon_{\min}$. The orange data points in Fig. 8(b) represent high-reflectivity roofs in the scene. A majority of these surfaces deviate from the MMD relationship, with only a minority exhibiting conformity. It is evident that metal surface poses a significant challenge in the retrieval of LST using the TES-MP algorithm. With the increasing urbanization, a growing variety of new building materials are being employed in urban construction. Therefore, it is essential to investigate the impact of these new building materials on the accuracy of TES-MP algorithm retrievals of UST.

B. MP-TES Accuracy

In this section, the errors in the calculation of LSE and LST during DART validation were evaluated using the following methods:

$$\Delta\varepsilon = \varepsilon_T - \varepsilon_{\text{MP-TES}} \tag{10}$$

$$\Delta T = T_T - T_{\text{MP-TES}}. \tag{11}$$

Here, ε_T is an effective LSE. $\varepsilon_{\text{MP-TES}}$ is the LSE retrieved by TES-MP algorithm. T_T is the true surface temperature, while $T_{\text{MP-TES}}$ is the LST retrieved by TES-MP algorithm.

1) Evaluating TES-MP Algorithm With the DART Model: The Mong Kok scene was used to validate the TES-MP algorithm retrievals [Fig. 6(a)]. Fig. 9(a) shows that TES-MP algorithm retrieves LST more accurately in the isothermal scene, where all element temperatures were set to 300 K (RMSE = 0.68 K), compared to the nonisothermal scene (RMSE = 0.75 K) with randomly assigned temperatures. The RMSE of the nonisothermal scene and isothermal scene in the first band is 0.011. The RMSE of the nonisothermal scene in the second band is 0.009, and that of the isothermal scene is 0.01. The RMSE of the nonisothermal scene and the isothermal scene in the third band is 0.009. The RMSE of LSE differences between nonisothermal and isothermal scenes is negligible across all three bands. Nevertheless, further sensitivity analysis remains necessary for comprehensive validation. Fig. 9 shows that there are occurrences of both overestimation and underestimation of LSE, which also lead to underestimation and overestimation of retrieved LST. The retrieval errors of LSE in the three bands are within 0.01 in most cases. Some LSEs seem to be significantly overestimated, which led to an underestimation of their LSTs. This is because materials with high reflectivity do not fit the MMD relationship.

The study area in Mong Kok is not flat, so the effective emissivity calculations have accounted for geometry effects, warranting a discussion of the sensitivity of TES-MP algorithm to geometric characteristics. The TES-MP algorithm exhibits relatively small retrieval errors of normal materials. However, it shows significantly larger retrieval errors for high-reflectivity materials.

It is necessary to seek more complex geometries to explore the applicability of TES-MP algorithm under both isothermal and nonisothermal conditions. Since the heterogeneity in the validation scene was not large, TES-MP algorithm was subsequently implemented in the Sheung Wan case for additional evaluation.

2) Validating TES-MP Algorithm With ECOSTRESS TIR: The LST from ECOSTRESS was acquired at 20:37, while that from SDGSAT-1 was obtained at 21:13. Since LST changes slowly during nighttime [24], the two datasets can be reliably compared. Fig. 10(c) shows good consistency between them. However, the LST retrieved from ECOSTRESS is higher than that from SDGSAT-1, which is also consistent with the time difference [Fig. 10(a) and (b)]. The BIAS is −0.63 K, indicating that the SDGSAT-1 LST is slightly lower than ECOSTRESS LST. The RMSE between the two datasets is 1.43 K, and the mean absolute error (MAE) is 1.1 K [Fig. 10(c)]. Some large errors are primarily attributed to heterogeneity in surface cooling efficiency, along with inherent errors in the algorithm. The spatial texture of the SDGSAT-1 LST is superior to that of ECOSTRESS, primarily due to its higher spatial resolution. Therefore, the TES-MP algorithm is considered feasible.

C. TES-MP Algorithm Applications

We analyzed three TIR images of the lower Pearl River Delta, which include two nighttime and one daytime image

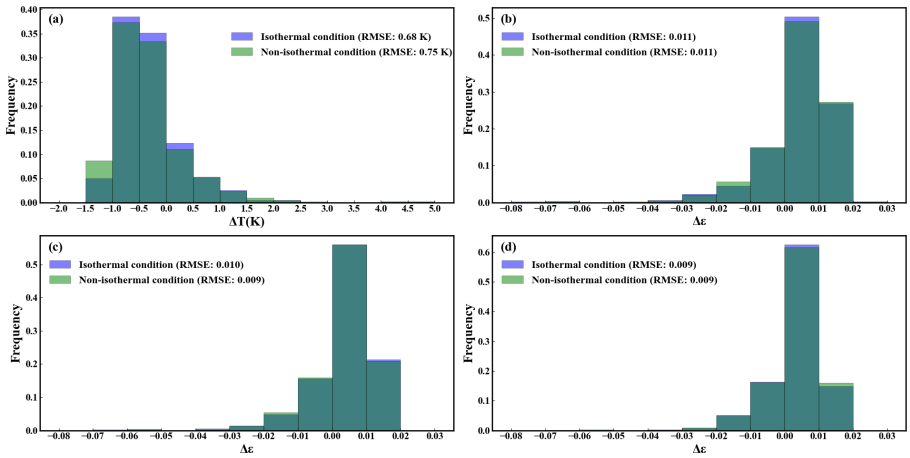

Fig. 9. Retrieval errors in LST and LSE for the three bands using the TES-MP algorithm: (a) LST error; (b) LSE error of the first band; (c) LSE error of the second band; and (d) LSE error of the third band.

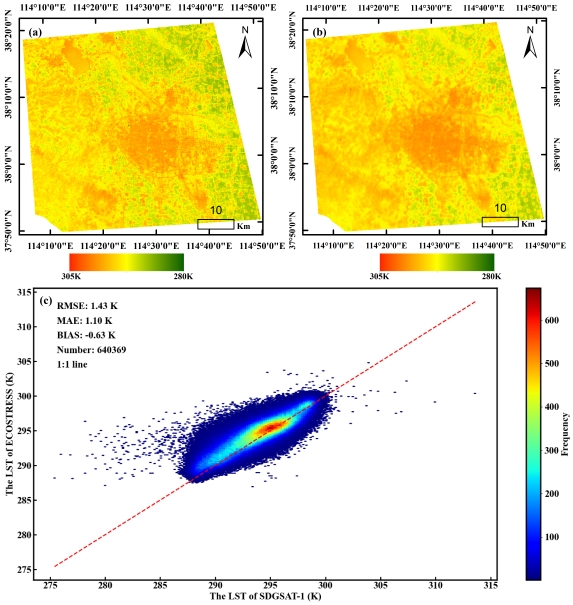

Fig. 10. LST on May 27, 2025: (a) SDGSAT-1 at 21:13; (b) ECOSTRESS at 20:37; and (c) comparison between ECOSTRESS and SDGSAT-1 LST.

(Fig. 11). The three plots in Fig. 11 demonstrate the differences in the timing and distribution of LST. Fig. 11 shows that SDGSAT-1 TIR captures LST patterns at a higher spatial resolution. Fig. 11(a)–(c) represents February nights, May nights, and December days, respectively. Overall, LST is higher on the east bank of the Pearl River than on the west bank. During the February night, the temperature of water bodies is higher than most land surfaces, while during the May night, the LST of the land surface is higher than that of the water bodies. Vegetation remains cooler at both times. The high-temperature zone on May nights is mainly concentrated in the western part of Shenzhen and Dongguan. Fig. 11(c) shows that during the day, the LST of impervious surfaces is higher than that of vegetation and water bodies. The temperature pattern is not uniform due to the heterogeneity in surface heat absorption. The LST at night in May is higher than the daytime LST in December. This is attributable to higher solar irradiance in May compared to December and reduced nocturnal surface heat dissipation efficiency. In December, solar radiation is weak during the day, leading to slower surface warming.

D. TES-MP Algorithm Sensitivity Under Thermal Heterogeneity Conditions

Section III-C.2 details the complete data processing chain for generating TIR image data under both isothermal and nonisothermal conditions within the same scene. Hong Kong's Sheung Wan was selected as the sensitivity analysis area for this study because its geometry is more complex.

Comparing the RMSE between Mong Kok (0.68 K) and Sheung Wan (0.85 K) under isothermal condition, we observe a significant increase in the RMSE in the Sheung Wan area, likely due to its more complex urban geometry and material proportion [Fig. 12(a)]. The RMSE in the Mong Kok scene (0.75 K) is slightly smaller than that in the Sheung Wan scene (1.13 K) under nonisothermal condition. This is partly due to the stronger LST heterogeneity in Sheung Wan compared to Mong Kok.

The nonisothermal LSE errors are significantly higher than the isothermal LSE errors. Specifically, the RMSE for the first band is 0.014 for the isothermal scene and 0.016 for the nonisothermal scene. For the second band, the RMSE is 0.012 for the isothermal scene and 0.014 for the nonisothermal scene. For the third band, the RMSE is 0.011 for the isothermal scene and 0.014 for the nonisothermal scene. Most of the LSE retrieval errors are concentrated within 0.02 or less. Compared to the Mong Kok scene (errors < 0.08), there is a noticeable increase in the Sheung Wan scene (errors < 0.11). This difference is partly attributable to variations in the percentage of high reflectivity material within the pixel. However, this effect requires further investigation. Second, the more complex urban geometry in Sheung Wan may contribute to this increase. It is evident that the impact of geometry on the TES-MP algorithm retrieval is less significant compared to the effect of high reflectivity. Under the isothermal condition, the RMSE of the TES-MP algorithm-retrieved LSE and LST is relatively small in both the Mong Kok and Sheung Wan scenes.

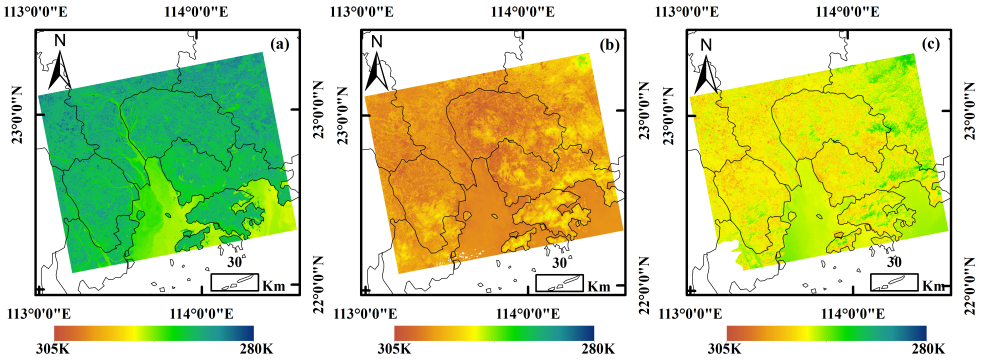

Fig. 11. LST: (a) February 10, 2024, 21:42; (b) May 16, 2024, 21:38; and (c) December 31, 2024, 09:56.

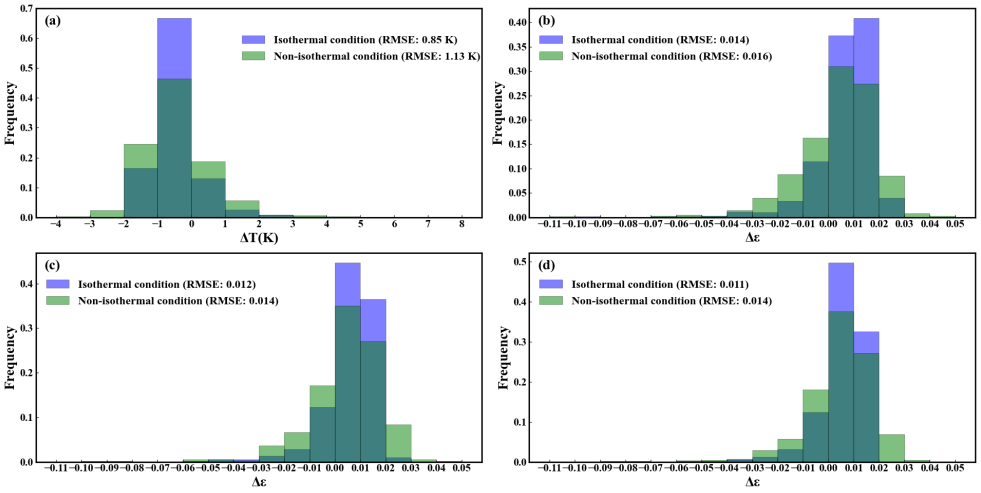

Fig. 12. Error analysis for isothermal and nonisothermal scenes: (a) LST error; (b) LSE error in the first band; (c) LSE error in the second band; and (d) LSE error in the third band.

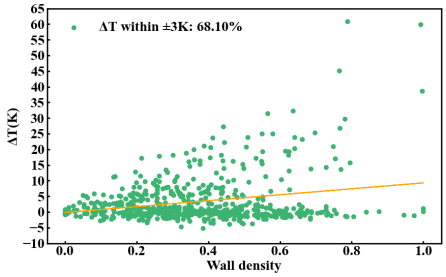

Fig. 13. LST retrieval error in the TES-MP algorithm at a zenith angle of 17°.

E. TES-MP Algorithm Sensitivity Under Different Observation Angles

To analyze the impact of observation angle on LST retrieval by the TES-MP algorithm, we set the observation zenith angle to 17°. This was chosen because the observation swath width of SDGSAT-1 is 300 km, and during vertical observation, the observation angle of the edge pixels is approximately 16°–17°. Under heterogeneous condition, temperatures and emissivities were the same as those in the nonisothermal scene of Sheung Wan.

Compared to nadir observations, the probability of observing a wall surface increases when the sensor is positioned at an oblique angle. Fig. 13 illustrates how LST retrieval error of the TES-MP algorithm varies with the proportion of wall area within pixels. In this study, 20 sets of reflectivity of walls were greater than 0.3, which explains the presence of some larger retrieval errors in Fig. 13. However, nearly 68.1% of the pixel errors remained within 3 K. This demonstrates that the TES-MP algorithm is adaptable to variations in viewing angle but exhibits limited adaptability to high-reflectivity surfaces.

F. TES-MP Algorithm Sensitivity Under Geometry Conditions

Section III-C.2 describes the approach to investigate the impact of adjacency effects. We assessed the impact of geometry characteristics on LST retrieval at 30-m resolution in this study. We combined the real directional emissivity with the DART-simulated emittance image for the third band (11.72 μm) and retrieved LST using the SC algorithm, which provided the LST without considering urban geometry. Subsequently, we utilized these data to estimate the error introduced by geometry and adjacency effects on LST retrieval. The LST error attributable to the adjacency effect was calculated by subtracting the LST retrieved using the SC algorithm, which includes geometry effects, from the LST retrieved using the SC algorithm without adjacency effects.

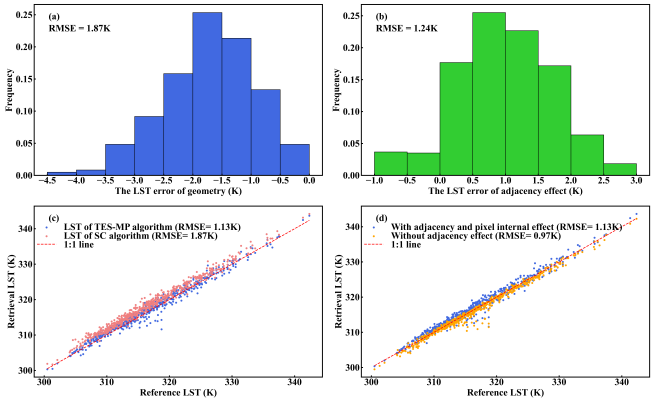

Fig. 14. Performance of TES-MP algorithm under geometry and adjacency effects: (a) error due to geometry effects; (b) error due to adjacency effects; (c) comparison of TES-MP and SC algorithm retrievals under geometry conditions; and (d) LST retrievals by TES-MP algorithm with and without adjacency effects.

Fig. 14(a) shows that the geometry effects introduce errors ranging from 0 to 4.5 K, with most occurrences concentrated around 0.5–3 K, and the RMSE of 1.87 K. This indicates that geometry has a significant influence on the retrieval of LST at a resolution of 30 m. The geometry effects include interactions between adjacency pixels and within pixels themselves, leading to an increase in exitance and subsequent errors in the LST retrieval.

Fig. 14(b) shows that the adjacency effects result in errors up to 3 K, with most errors falling within the 0–2 K range and an RMSE of 1.24 K, indicating a significant impact on retrieved LST. Variations in error also show that the extent of the adjacency effect is influenced by the geometry characteristics of adjacency pixels to the target.

Fig. 14(c) shows that TES-MP retrieval of LST remains close to the 1:1 line, achieving an RMSE of 1.13 K. This indicates that the TES-MP algorithm effectively mitigates the impact of geometry. Consequently, this highlights that the TES-MP algorithm possesses a certain degree of resistance to the effects of geometry characteristics.

Fig. 14(d) provides a detailed evaluation of the impact of the adjacency effect on LST retrieval using the TES-MP algorithm. When the adjacency effect is considered, the RMSE decreases to 0.97 K, as opposed to 1.13 K without considering it. This suggests that the TES-MP algorithm has a certain ability to remove adjacency effects. The improvement may be attributed to the fact that the TES-MP algorithm inherently incorporates the influence of adjacency effects in its retrieval process.

Fig. 14(c) shows that certain values of retrieved LST significantly deviate from the 1:1 line, which can be attributed to the presence of high reflectivity materials. Therefore, it is essential to further investigate the impact of these materials on the performance of the TES-MP algorithm.

G. TES-MP Algorithm Sensitivity Under High Reflectivity Conditions

The procedure for generating TIR images of scenes containing high-reflectivity surfaces is explained in Section III-C.2. High-reflectivity materials yield outliers of the MMD relationship when the TES-MP algorithm is applied. Given the frequent occurrence of high-reflectivity materials in the study area, we investigated the LST retrieval errors caused by these materials in walls and roofs.

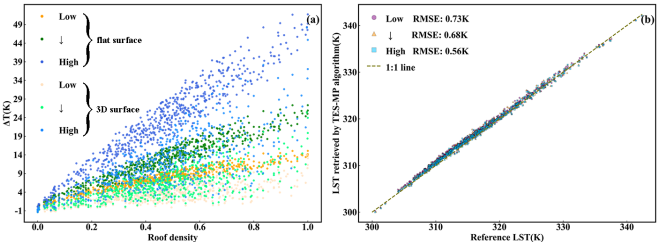

Fig. 15. Influence of high-reflectivity materials on TES-MP algorithm retrievals: (a) high-reflectivity roofs and (b) high-reflectivity walls.

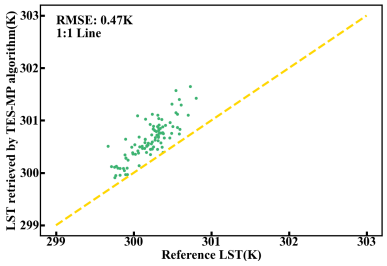

Fig. 16. LST retrieval error for vegetation areas using the TES-MP algorithm.

Fig. 15 shows that TES-MP algorithm underestimates LST when observing targets with high-reflectivity materials. The LST error increases as the percentage of high-reflectivity material increases when observing flat targets. In complex geometries, the LST error tends to decrease, but it remains significant. Higher wall reflectivity does not worsen the LST error; it tends to reduce it. However, this effect is only observed by the nadir view. This suggests that radiance received by the sensor from high-reflectivity targets influences LST retrieval, with the extent of the effect depending on the proportion of the targets within the pixel. The LST retrieval of high-reflectivity materials in complex urban areas exhibits greater uncertainty.

H. TES-MP Algorithm Sensitivity Under Vegetation Conditions

In this study, a 300 × 300 m simulated scene comprising only land surface and tree was created to investigate the sensitivity of the TES-MP algorithm in vegetation areas. The temperatures of the tree and ground were referenced to high-resolution datetime TIR data from Hong Kong in October 2017, and emissivities for both tree and ground were obtained from the ECOSTRESS spectral database. Tree was randomly distributed across the scene, with a maximum of 4000 trees generated due to computational constraints.

Fig. 16 illustrates that the TES-MP algorithm tends to overestimate temperature retrievals in vegetation areas. This suggests that the minimum emissivity of vegetation lies above the MMD curve, but the TES-MP MMD relationship to underestimate emissivity in these areas. However, the RMSE for LST retrieval by TES-MP is 0.47 K, indicating relatively small

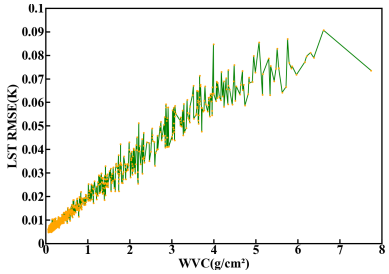

Fig. 17. RMSE between LST retrieved by the TES-MP algorithm with and without atmospheric errors varies with WVC.

retrieval errors and confirming the algorithm's applicability to vegetated areas.

I. TES-MP Sensitivity Under Different Atmospheric Conditions

In this study, TIGR was used to analyze the sensitivity of the TES-MP algorithm under different atmospheric conditions. MODTRAN5.2 was employed to calculate $R^{\uparrow}_{\text{atm}}$, $R^{\downarrow}_{\text{atm}}$, and τ. Concurrently, ten material samples and different LSTs were used to calculate surface-leaving radiance. These LSTs were set as LST = T_a + ΔT, where T_a was the lowest layer LST of TIGR, where ΔT was the temperature change ranging from −20 to 25 K at a step of 5 K [39]. We introduced 5% Gaussian noise to $R^{\downarrow}_{\text{atm}}$, analyzing atmospheric errors [13].

Fig. 17 shows that the RMSE is lower by 0.1 K between LST retrieved by the TES-MP algorithm with and without 5% Gaussian noise of $R^{\downarrow}_{\text{atm}}$. As WVC increases, the RMSE increases. Therefore, the impact of WVC on LST retrieved by the TES-MP algorithm is relatively minor, assuming that the atmospheric parameters are reasonably accurate.

V. Discussion

SDGSAT-1 retrieves LST at a higher spatial resolution compared to other current spaceborne sensor systems in the TIR band. Despite the high heterogeneity of urban materials, the TES-MP algorithm can retrieve LST with minimal errors. We simulated TIR scenes, including high-reflectivity roofs and walls under both isothermal and nonisothermal conditions. Adjacency effects under nonisothermal conditions were modeled. We analyzed the LST retrieval errors of the TES-MP algorithm at an observed zenith angle of 17°. We analyzed the LST retrieval errors of the TES-MP algorithm in vegetation areas. We evaluated the LST error retrieved by the TES-MP algorithm under different WVC conditions, accounting for uncertain atmospheric parameters, using MODTRAN.

The TES-MP algorithm yields relatively small errors in LST retrieval for the isothermal scene; however, the error increases significantly when nonisothermal pixels are considered [40]. Specifically, nonisothermal pixels tend to induce larger LST errors when retrieved by the TES-MP algorithm, compared to isothermal pixels, with the difference typically being around 2 K or less. Additionally, LST errors may further increase when the sensor detects substantial LST variations within a pixel. This is attributed to the uncertainty associated with thermal radiance heterogeneity caused by variations in LST. Overall, the TES-MP algorithm exhibits relatively minimal LST errors in most pixels.

Cavity effects pose significant challenges in retrieving the LST in complex scenes [14]. The change from a flat surface to a 3-D structure increases radiance due to multiple scattering and reflections from the interior. The increase in radiance can cause significant error when using the traditional SC algorithm retrieval for LST without considering geometry. In contrast, TES-MP algorithm retrievals of LST exhibit relatively small error. This demonstrates that the TES-MP algorithm can reduce the impact of errors in LST caused by geometry-induced emissivity variations.

The effect of adjacency pixels increases with increasing resolution [41], further demonstrating that adjacency effects scale with both increasing spatial resolution and geometric complexity of surrounding pixels. Higher resolution amplifies the impact of nontarget pixel geometry. Under nonisothermal conditions at 30-m resolution, the maximum adjacency-induced error reaches 3 K, while most errors remain within 2 K. As shown in Fig. 14(d), accounting for adjacency effects reduces the LST RMSE derived from the TES-MP algorithm from 1.13 to 0.97 K. This suggests that the TES-MP algorithm should account for and mitigate the effect of adjacency effects. However, in the absence of high-accuracy DSM data, the TES-MP algorithm can still achieve good results without considering the adjacency effect.

Even in nadir observation, the satellite's observation angle can remain large at the edges of pixels. Research indicates that the TES-MP algorithm can still retrieve LST with relatively small errors when the satellite is at an oblique angle. In most cases, the satellite observation angle has a minor impact on LST retrieval. Instead, error variations depend more on the characteristics of the observed surface.

MPs also satisfy the relationship between MMD and $\varepsilon_{\min}$. TES-MP algorithm is suitable for most low-reflectivity materials and retrieves LST with relatively small errors. However, it cannot accurately retrieve for all surfaces. High-reflectivity surfaces cannot be correctly retrieved, leading to very large errors and underestimation of LST. The emissivity of metal surfaces does not fit the MMD relationship required for applying the TES algorithm [42], [43]. Michel et al. [42] showed that the TES algorithm performs poorly on metals and gives outliers when estimating the MMD relationship.

As the proportion of high-reflectivity materials within a pixel increases, the error in LST retrieval correspondingly increases. Complex geometries induce multiple scattering and reflection events, thereby elevating the effective emissivity of high-reflectivity surfaces. When such surfaces reflect signals from surrounding surfaces with higher temperatures, their effective emissivity may exceed 1. While this phenomenon partially mitigates LST retrieval errors compared to those associated with flat surfaces, the substantial radiance originating from the surrounding environment also increases the uncertainty in LST retrieval results obtained using the TES-MP algorithm. TIR observations primarily capture radiance emitted by objects themselves and reflected environmental radiance [4]. During nadir observation, the TIR signal mainly originates from grounds, roofs, and partially scattered wall radiance [44]. As the emissivity of the grounds and roofs

approaches 1, the greater the reflectivity of the walls, the weaker their influence on the grounds and roofs becomes. This indicates a reduced impact of ambient radiance in the observation direction. This explains why Fig. 15(b) shows that the LST retrieval error of the TES-MP algorithm decreases with increasing wall reflectivity during nadir observations.

The accuracy of the TES-MP algorithm also depends on the precise estimation of atmospheric parameters [1]. In humid regions, uncertain atmospheric parameters significantly affect retrieved LST using the TES-MP algorithm [11], [45]. However, when uncertain atmospheric parameters are minimal, the resulting retrieval errors are relatively minor.

From the results, it can be observed that the TES-MP algorithm effectively mitigates the impact of geometry and adjacency effects through iterations with the three major modules. The LST error retrieved by the TES-MP algorithm is larger under the nonisothermal condition than under the isothermal condition; however, TES-MP algorithm has further reduced this error. The TES-MP algorithm tends to overestimate temperatures in vegetation areas although the overall error remains relatively small. It exhibits low sensitivity to variations in observation angle and to a 5% uncertainty in atmospheric parameters. However, high-reflectivity materials (e.g., metals) lead to outliers in the MMD and $\varepsilon_{\min}$ curves and are the primary cause of large LST errors. Overall, the TES-MP algorithm effectively demonstrates its advantages in retrieving LST, provided that at least three spectral TIR channels are available. The TES-MP algorithm developed in this study integrates 3-D building geometry, tree effects, and varying temperatures and emissivities during the DART modeling process, making it applicable for LST retrieval in the vast majority of urban areas.

For the study of the urban thermal environment, a complete UST is more meaningful than directional LST [44]. However, this study focused on the directional LST retrieval, and the development of a complete surface temperature retrieval method will be considered in the future.

The DART model contains errors. Assigning the same temperature to the walls and roofs of buildings in Mong Kok and Sheung Wan areas is overly idealized for validation in real-world conditions. The shaded and sunny sides of each urban object vary, leading to significant temperature fluctuations, even within small areas. This study primarily focuses on MPs; therefore, the LST retrievals from PPs using the TES-MP algorithm may introduce significant errors.

VI. Conclusion

In this study, MP scenes were constructed utilizing the DART model to establish a new relationship between MMD and $\varepsilon_{\min}$ for retrieving UST with SDGSAT-1 TIR data. Due to complex geometry and the absence of on-site measurements, DART was employed to validate retrieved LST and LSE, while ECOSTRESS TIR was used to validate retrieved LST. The following conclusions were drawn based on the results.

1) Based on the results of the DART validation study, the RMSE of LST retrievals by the TES-MP algorithm in heterogeneous conditions is 0.75 K, with most errors within 1 K. Compared to other bands (RMSE < 0.011), the first band achieves the highest RMSE of 0.011 in LSE retrieval. In future studies, this algorithm will be validated with on-site measurements.
2) Under more complex geometry conditions, the RMSE of retrieved LST for TES-MP is 1.13 K. This means that the TES-MP algorithm can be applied to retrieve UST.
3) Changes in the observation angle increase the proportion of interior walls within pixels but do not affect the error in LST retrieval by the TES-MP algorithm, as long as the observed surface satisfies the MMD relationship.
4) It is well-known that the adjacency and geometry have a significant effect on the observed TIR exitance. However, the TES-MP algorithm effectively mitigates the geometry and adjacency effects to some extent. We recommend that multiple spectral bands ($\geq$ 3) should be implemented when designing TIR sensors.
5) The accuracy of the retrieved LST using the TES-MP algorithm is highly susceptible to high-reflectivity materials. In most cases, metals do not conform to the relationship between MMD and $\varepsilon_{\min}$. Furthermore, the higher the reflectivity of materials, the larger the LST error becomes. In urban areas with complex geometries, the error may be somewhat reduced, but uncertainty still persists. When metal surfaces are not observed (i.e., when the wall is highly reflective and under nadir observation), the accuracy of LST is not significantly affected, and the error may even be reduced.
6) The TES-MP algorithm remains applicable in vegetation areas but may overestimate vegetation temperatures.
7) Accurate atmospheric correction parameters can minimize errors in LST retrieval, particularly in humid regions.

Acknowledgment

The research findings are a component of the SDGSAT-1 Open Science Program, which is conducted by the International Research Center of Big Data for Sustainable Development Goals (CBAS). The data utilized in this study are sourced from SDGSAT-1 and provided by CBAS.

References

[1] Z.-L. Li et al., "Satellite-derived Land Surface Temperature: Current status and perspectives," *Remote Sens. Environ.*, vol. 131, pp. 14–37, Apr. 2013.

[2] X. Ouyang, Z. Sun, S. Zhou, and Y. Dou, "Urban Land Surface Temperature retrieval with high-spatial resolution SDGSAT-1 thermal infrared data," *Remote Sens. Environ.*, vol. 312, Oct. 2024, Art. no. 114320.

[3] J. Cheng et al., "A global 1 km resolution daily surface longwave radiation product from MODIS satellite data from 2000–2023," *Sci. Data*, vol. 12, no. 1, p. 736, May 2025.

[4] S. Chen, H. Ren, X. Ye, J. Dong, and Y. Zheng, "Geometry and adjacency effects in urban Land Surface Temperature retrieval from high-spatial-resolution thermal infrared images," *Remote Sens. Environ.*, vol. 262, Sep. 2021, Art. no. 112518.

[5] X. Guo et al., "Global patterns and determinants of year-to-year variations in surface urban heat islands," *ISPRS J. Photogramm. Remote Sens.*, vol. 223, pp. 399–412, May 2025.

[6] L. Wei and J. A. Sobrino, "Surface urban heat island analysis based on local climate zones using ECOSTRESS and Landsat data: A case study of Valencia city (Spain)," *Int. J. Appl. Earth Observ. Geoinf.*, vol. 130, Jun. 2024, Art. no. 103875.

[7] C. Li et al., "LFSR: Low-resolution filling then super-resolution reconstruction framework for gapless all-weather MODIS-like Land Surface Temperature generation," *Remote Sens. Environ.*, vol. 319, Mar. 2025, Art. no. 114637.
[8] X. Zheng, Y. Guo, Z. Zhou, and T. Wang, "Improvements in Land Surface Temperature and emissivity retrieval from Landsat-9 thermal infrared data," *Remote Sens. Environ.*, vol. 315, Dec. 2024, Art. no. 114471.
[9] M. Xiao, S. Zhou, and J. Cheng, "Comparison of three temperature and emissivity separation algorithms for graybodies with low spectral contrast: A case study on water bodies," *Remote Sens.*, vol. 17, no. 3, p. 455, Jan. 2025.
[10] S. Wang, J. Cheng, and Q. Liu, "Study on the effect of shortwave radiation in Land Surface Temperature downscaling over rugged terrain," *Remote Sens.*, vol. 17, no. 14, p. 2436, Jul. 2025.
[11] Z.-L. Li et al., "Land surface emissivity retrieval from satellite data," *Int. J. Remote Sens.*, vol. 34, nos. 9–10, pp. 3084–3127, May 2013, doi: 10.1080/01431161.2012.716540.
[12] H. Li et al., "Evaluation of the VIIRS and MODIS LST products in an arid area of Northwest China," *Remote Sens. Environ.*, vol. 142, pp. 111–121, Feb. 2014.
[13] Y. Teng, H. Ren, Y. Hu, and C. Dou, "Land Surface Temperature retrieval from SDGSAT-1 thermal infrared spectrometer images: Algorithm and validation," *Remote Sens. Environ.*, vol. 315, Dec. 2024, Art. no. 114412.
[14] J. Yang, M. S. Wong, M. Menenti, and J. Nichol, "Study of the geometry effect on Land Surface Temperature retrieval in urban environment," *ISPRS J. Photogramm. Remote Sens.*, vol. 109, pp. 77–87, Nov. 2015.
[15] J. Yang et al., "Development of an improved urban emissivity model based on sky view factor for retrieving effective emissivity and surface temperature over urban areas," *ISPRS J. Photogramm. Remote Sens.*, vol. 122, pp. 30–40, Dec. 2016, doi: 10.1016/j.isprsjprs.2016.09.007.
[16] S. Chen et al., "Urban Land Surface Temperature retrieval from high spatial resolution thermal infrared image using a modified split-window algorithm," *IEEE Trans. Geosci. Remote Sens.*, vol. 61, 2023, Art. no. 5003216, doi: 10.1109/TGRS.2023.3291708.
[17] Q. Mao, J. Peng, and Y. Wang, "Resolution enhancement of remotely sensed Land Surface Temperature: Current status and perspectives," *Remote Sens.*, vol. 13, no. 7, p. 1306, 2021.
[18] W. Liu and J. Cheng, "The first result of Land Surface Temperature retrieval from SDGSAT-1 thermal imager spectrometer," *IEEE Geosci. Remote Sens. Lett.*, vol. 21, pp. 1–5, 2024.
[19] M. Wu, J. Wu, and C. Zang, "A comprehensive evaluation of the eco-carrying capacity and green economy in the guangdong-hong kong-macao greater bay area, China," *J. Cleaner Prod.*, vol. 281, Jan. 2021, Art. no. 124945.
[20] H. Guo et al., "SDGSAT-1: The world's first scientific satellite for sustainable development goals," *Sci. Bull.*, vol. 68, no. 1, pp. 34–38, Jan. 2023.
[21] J. B. Fisher, "ECOSTRESS: NASA's next generation mission to measure evapotranspiration from the international space station," *Water Resour. Res.*, vol. 55, no. 5, pp. 3180–3191, May 2019.
[22] S. Hook and G. Hulley. (2022). *ECOSTRESS Tiled Land Surface Temperature and Emissivity Instantaneous L2 Global 70 m v002 [Data set]*. NASA Land Processes Distributed Active Archive Center. [Online]. Available: https://doi.org/10.5067/ECOSTRESS/ECO_L2T_LSTE.002
[23] G. C. Hulley et al., "Validation and quality assessment of the ECOSTRESS level-2 Land Surface Temperature and emissivity product," *IEEE Trans. Geosci. Remote Sens.*, vol. 60, pp. 1–23, 2022.
[24] W. Wang, S. Liang, and T. Meyers, "Validating MODIS Land Surface Temperature products using long-term nighttime ground measurements," *Remote Sens. Environ.*, vol. 112, no. 3, pp. 623–635, Mar. 2008.
[25] S. K. Meerdink, S. J. Hook, D. A. Roberts, and E. A. Abbott, "The ECOSTRESS spectral library version 1.0," *Remote Sens. Environ.*, vol. 230, Sep. 2019, Art. no. 111196.
[26] S. Kotthaus, T. E. L. Smith, M. J. Wooster, and C. S. B. Grimmond, "Derivation of an urban materials spectral library through emittance and reflectance spectroscopy," *ISPRS J. Photogramm. Remote Sens.*, vol. 94, pp. 194–212, Aug. 2014.
[27] H. Hersbach et al., "ERA5 hourly data on pressure levels from 1940 to present, Copernicus climate change service (C3S) climate data store (CDS)," 2023, doi: 10.24381/cds.bd0915c6.
[28] N. Wang, J. Tian, S. Su, and Q. Tian, "A downscaling method based on MODIS product for hourly ERA5 reanalysis of Land Surface Temperature," *Remote Sens.*, vol. 15, no. 18, p. 4441, Sep. 2023.
[29] F. Chevallier, F. Chéruy, N. A. Scott, and A. Chédin, "A neural network approach for a fast and accurate computation of a longwave radiative budget," *J. Appl. Meteorol.*, vol. 37, no. 11, pp. 1385–1397, Nov. 1998.
[30] B.-H. Tang, "Nonlinear split-window algorithms for estimating land and sea surface temperatures from simulated Chinese Gaofen-5 satellite data," *IEEE Trans. Geosci. Remote Sens.*, vol. 56, no. 11, pp. 6280–6289, Nov. 2018.
[31] S. Zhou and J. Cheng, "A physics-based atmospheric precipitable water vapor retrieval algorithm by synchronizing MODIS near-infrared and thermal infrared measurements," *Remote Sens. Environ.*, vol. 317, Feb. 2025, Art. no. 114523.
[32] A. Gillespie, S. Rokugawa, T. Matsunaga, J. S. Cothern, S. Hook, and A. B. Kahle, "A temperature and emissivity separation algorithm for Advanced Spaceborne Thermal Emission and Reflection Radiometer (ASTER) images," *IEEE Trans. Geosci. Remote Sens.*, vol. 36, no. 4, pp. 1113–1126, Jul. 1998.
[33] Z.-L. Li et al., "Satellite remote sensing of global Land Surface Temperature: Definition, methods, products, and applications," *Rev. Geophys.*, vol. 61, no. 1, Mar. 2023, Art. no. e2022RG000777, doi: 10.1029/2022RG000777.
[34] Y. Wang and J.-P. Gastellu-Etchegorry, "DART: Improvement of thermal infrared radiative transfer modelling for simulating top of atmosphere radiance," *Remote Sens. Environ.*, vol. 251, Dec. 2020, Art. no. 112082.
[35] Y. Wang et al., "DART-lux: An unbiased and rapid Monte Carlo radiative transfer method for simulating remote sensing images," *Remote Sens. Environ.*, vol. 274, Jun. 2022, Art. no. 112973.
[36] Z. Bian et al., "An analytical urban temperature model with building heterogeneity using geometric optical theory," *Remote Sens. Environ.*, vol. 301, Feb. 2024, Art. no. 113948.
[37] Z. Zhen et al., "A gradient-based 3D nonlinear spectral model for providing components optical properties of mixed pixels in shortwave urban images," *Remote Sens. Environ.*, vol. 321, May 2025, Art. no. 114657.
[38] Z. Wang et al., "Modelling and optimizing tree planning for urban climate in a subtropical high-density city," *Urban Climate*, vol. 43, May 2022, Art. no. 101141.
[39] H. Zeng, H. Ren, J. Nie, J. Zhu, X. Ye, and C. Jiang, "Land Surface Temperature and emissivity retrieval from nighttime middle and thermal infrared images of Chinese fengyun-3D MERSI-II," *IEEE J. Sel. Topics Appl. Earth Observ. Remote Sens.*, vol. 14, pp. 7724–7733, 2021.
[40] Y. Du et al., "An experimental study on separating temperature and emissivity of a nonisothermal surface," *IEEE Geosci. Remote Sens. Lett.*, vol. 16, no. 10, pp. 1610–1614, Oct. 2019.
[41] X. Zheng, Z.-L. Li, X. Zhang, and G. Shang, "Quantification of the adjacency effect on measurements in the thermal infrared region," *IEEE Trans. Geosci. Remote Sens.*, vol. 57, no. 12, pp. 9674–9687, Dec. 2019.
[42] A. Michel et al., "A new material-oriented TES for Land Surface Temperature and SUHI retrieval in urban areas: Case study over Madrid in the framework of the future TRISHNA mission," *Remote Sens.*, vol. 13, no. 24, p. 5139, Dec. 2021.
[43] J. A. Sobrino et al., "Emissivity mapping over urban areas using a classification-based approach: Application to the dual-use European security IR experiment (DESIREX)," *Int. J. Appl. Earth Observ. Geoinformation*, vol. 18, pp. 141–147, Aug. 2012.
[44] J. Yang et al., "A semi-empirical method for estimating complete surface temperature from radiometric surface temperature, a study in Hong Kong city," *Remote Sens. Environ.*, vol. 237, Feb. 2020, Art. no. 111540.
[45] W. Liu, J. Cheng, and L. Dong, "Land Surface Temperature retrieval from FY-3E/MERSI using an optimized water vapor scaling method," *GIScience Remote Sens.*, vol. 62, no. 1, Dec. 2025, Art. no. 2507439.